Supporting Information

Enhanced Organic Solar Cells Efficiency through Electronic and Electro-optic Effects Resulting from Charge Transfers in Polymer Hole Transport Blends

1. Experimental Section

1.1. Materials

Hydrochloric acid (HCl, 37 %), acetone, isopropanol, dichlorobenzene, chlorobenzene were all HPLC grade and purchased from Sigma-Adrich. Perfluorinated ionomer resin solution (PFI, Nafion® DE 520, 5 wt. % in an alcohols and aqueous solution including 45 % of water, with a density of 0.924 g/mL at 25 °C) and perfluoro-octane sulfonic acid solution (FOS, M_w = 500.13, D, ~ 40 % in water with 1.25 g/mL density) were also from Sigma-Adrich. 1, 8-diiodooctane (DIO) was from Fluka. Poly(3, 4-ethylenedioxythiophene: poly (styrenesulfonate) (PEDOT:PSS, 1:6 weight ratio, 1 g/L ; AI4083) was from Clevios, poly({4,8-bis[(2-ethylhexyl)oxy]benzo[1,2-b:4,5 b']dithiophene-2,6-diyl}{3-fluoro-2-[(2-ethylhexyl)carbo-nyl]thieno[3,4-b] thiophenediyl})) (PTB7, M_w = 92 kDa, pdi = 2.6) was from 1-Material; regioregular poly(3-hexylthiophene) (P3HT, M_w = 57 kDa, pdi = 2.9) was from Rieken Metals. The soluble fullerenes [6,6]-phenyl-C_{60}/C_{70} butyric acid methyl ester ($PC_{60}BM$ / $PC_{70}BM$) were both purchased from Solenne (99 % purity).

Indium tin oxide (ITO) coated glass substrates (15 Ω/square) were purchased from Xin Yan Technology Ltd. UV optical adhesive (Norland Optical Adhesive 68) and glass coverslips used for the encapsulation were purchased from Thorlabs and Fisher Scientific, respectively.

1.2. Device Fabrication

An adhesive tape was used as a mask of the ITO-coated glass substrates, which were etched in HCl (37 %) for 20 min. The mask was removed and further cleaning of the substrates was completed by sonication in deionized water, acetone and isopropanol. The substrates were then dried with a nitrogen flow before being treated in an oxygen plasma asher for 5 min.

Solutions with 6:1:30 weight ratio of PEDOT:PSS:fluorinated agent (FA) were prepared based on the weight concentration of the material indicated by the manufacturers (1 wt %, 5 wt% and 40 wt% for PEDOT: PSS, PFI and FOS respectively). The PEDOT:PSS, the PFI and FOS solutions were used as received. The volumes of the fluorinated agent solution (~ 278 µL and ~ 25 µL for PFI and FOS respectively) were added to 3 mL of PEDOT:PSS solution and left overnight under vigorous stirring. Before use, the solutions were sonicated, filtered (pore size 0.45 µm) and spin-coated at ~ 4 k.rpm to form 40 nm thick films on quartz substrates. With a a hotplate placed in a nitrogen-filled glovebox, the PEDOT:PSS:FA-coated ITO substrates were subsequently annealed at 120 °C for 15 min.

The liphophilic organic semiconductors were dissolved by gentle stirring in a N_2-filled glove-box: PTB7: $PC_{70}BM$, 5:7.5 mg in 0.5 mL, were dissolved in *ortho*-dichlorobenzene at 50 °C for a few hours. After the solution was cooled down to room-temperature, 3 % v/v DIO was added to the solution, which was left to stir for further 5 min before being spin-coated at 1 k.rpm to obtain a ~100 nm thick film; P3HT:$PC_{60}BM$ 5:5 mg were dissolved in 0.5 mL chlorobenzene and stirred overnight at 70 °C. The solution was spin-coated at 1 k.rpm on top of the annealed PEDOT:PSS based layer. The ~80nm thick P3HT:$PC_{60}BM$ based devices were then annealed under inert and dry atmosphere at 130 °C for 15 min.

The top electrode was evaporated under a 2.10⁻⁶ mBar vacuum: P3HT:$PC_{60}BM$ was coated with a 200 nm thick aluminum layer, while PTB7:$PC_{70}BM$ was covered first by a 20 nm calcium layer on-top of which a 200 nm aluminum layer was evaporated. PTB7:$PC_{70}BM$ devices were immediately removed from the evaporator and encapsulated with a UV optical adhesive and a glass coverslip, whilst P3HT:$PC_{60}BM$ devices were not encapsulated. Devices were then removed from the glovebox, masked and characterized in air with a Keithley 2400 source-measure unit and a K.H. Steuernagel AM1.5G solar simulator providing an illumination intensity of 100 mWcm² verified with an NREL-calibrated monosilicon detector and a KG-5 filter. The solar cell area was 0.08 cm² and their characteristics were extracted from the J-V curves with the power conversion efficiency (*PCE* or *η*) determined with the standard following equation

$$\eta = \frac{V_{OC}I_{SC}FF}{P_{in}} \tag{1}$$

where V_{OC} is the open-circuit voltage, I_{SC} the short-circuit

current, *FF* the fill factor, and P_{in} the incident light power. The external quantum efficiency (*EQE*) was measured with an incident photon to charge carrier efficiency setup, made of an NPL-calibrated photodiode, a Keithley 6517A picoammeter and a TMc300 monochromator.

1.3. Characterisation Techniques
1.3.1. Topography and Kelvin Probe Measurements
The surface work function of the sample was measured using a scanning probe microscopy (SPM) system (XE-100, Park Systems Co.) with a controlled glove box environment. All the measurements were performed under N_2 atmosphere and ambient temperature. The samples were heated at 120 °C for 20 min to remove water adsorbates just prior to the SPM experiments. Conductive Pt-coated Si cantilevers (NT-MDT) were used for the measurements. The topography was obtained using AC mode with a resonance frequency of 280 kHz. KPFM images were simultaneously acquired by applying to the tip an AC modulation voltage of 2 V amplitude and 20 kHz frequency. For the estimation of the sample work function, the Pt coated tip (4.7 eV) was calibrated with the highly ordered pyrolytic graphite (HOPG) reference sample.

To extract the work function ($W_{f\text{-KPFM}} = W_{sample}$) from the data, first the contact potential difference (V_{CPD}) was measured, and then the work function of the SPM tip (W_{tip}) was calibrated. Finally, $W_{f\text{-KPFM}}$ of the sample was deduced from the equation (2), with q the electronic charge of an electron.[1-3]

$$V_{CPD} = \frac{(W_{tip} - W_{sample})}{q} \qquad (2)$$

1.3.2. Macroscopic Kelvin Probe Measurements
As described in section 1.2, the PEDOT:PSS-based films were prepared on ITO substrates by spin-coating. The samples were then annealed at 120 °C for 15 min on a hot plate in a N_2-filled glove-box. The work function of the film was then measured using a Kelvin probe (FAC-1, RIKEN KEIKI) with a measured area of 1 cm in diameter. The calibration was carried out by gold thin plates giving a 5.10 eV value.

1.3.3. Conductivity Measurements
The pristine and fluorinated PEDOS:PSS films were prepared by spin-coating and thermal annealing, as described above but these steps were repeated three consecutive times to form thicker films required for reliable measurements. Once the thick films obtained, thermal annealing was completed for 20 min. The prepared PEDOT:PSS films were ~100 nm thick for the pristine film, ~250 nm for the PFI-based film, and ~85 nm for the FOS-based film, respectively. Gold was then deposited onto each sample through a shadow mask with a pattern of two contact pads. The contact length and width of the two contact pads were 8.5 mm and 3.0 mm, respectively. After cutting the part which is not to be measured in each sample (i.e., outside of the two contact pads), the sheet resistance and conductivity between the two contact pads were determined using an Agilent B1500A semiconductor device analyzer in a N_2-filled glove-box.

For the post spin-coating treatments with pure organic solvents, chlorobenzene and di-chlorobenzene solvents were individually spin-coated at 1 k.rpm onto the pristine and fluorinated films prepared with the same procedure. The post spin-coating treatments were performed before the deposition of the gold contact pads, and the samples

were left at room temperature in a N_2-filled glove-box and overnight for the solvent to evaporate.

1.3.4. Transient Absorption Spectroscopy
Femtosecond transient absorption measurements were carried out using pump and probe pulses generated by a Ti:Sapphire regenerative amplifier (Spitfire Pro XP, Spectra-Physics) working with an 800 nm output. A Mai Tai laser composed of a mode-locked Titanium-doped sapphire (Ti^{3+}:Al_2O_3) laser (Tsunami) and of a diode-pumped continuous wave Nd:YVO$_4$ laser (Millennia). The former was used as the seeding laser for the regenerative amplifier. The latter was used to pump the Tsunami. The regenerative amplifier was based on a Q-switched intra-cavity frequency doubled Nd:YLF laser operating at a repetition rate of 5 kHz and delivered 40 fs long pulse centered at 800 nm. The beam was split into two. The first led to the 400 nm pumping beam obtained by second harmonic generation using a beta barium borate (BBO) crystal after the Ti:Sapphire regenerative amplifier. The pump beam was attenuated to 1.0 mW using neutral density filters located in front of the sample. The second beam was directed to a 2 mm thickness sapphire crystal to generate a white light continuum in the visible range from which the 640 nm probe beam was selected. The time delay between the pump and probe beam was varied up to 500 ps using a delay line. The time intervals for the on-set and decay measurements were 100 fs and 5 ps in stepping motor, respectively. Pump light was modulated using a mechanical chopper at 220 Hz and the differential transmission *ΔT/T* of the probe beam was determined as a function of the delay time with a detection setup including photodiode and lock-in. A filter cutting the light below 635 nm was used to reduce the potential impact of scattered light from the pump beam. The pump ($\lambda = 400$ nm, $P \sim 1$ mW, $\phi \sim 0.5$ mm) and probe ($\lambda = 640$ nm, $P \sim 0.01$ mW, $\phi \sim 10$ μm) beams hit the substrates on the polymer side and the differential transmission was calculated as

$$\Delta T/T(\lambda, t) = [T_{on}(\lambda, t) - T_{off}(\lambda, t)]/T_{off}(\lambda, t) \qquad (3)$$

where T_{on} and T_{off} correspond to the sample transmission with the pump beam on and off, respectively. The charge separation (i.e. onset, rise) and recombination (i.e. decay, recovery) times were measured with 100 fs and 10 ps time interval, respectively. The values were extracted from the *ΔT/T* curves plotted as a function of the delay time and fitted with eqs. (9) and (10), respectively.

$$\Delta T/T(t) = \alpha.[1 - \exp(-t/\tau_{CS})] \qquad (4)$$

$$\Delta T/T(t) = -\alpha.\exp(-t/\tau_{CR}) \qquad (5)$$

1.3.5. Optical Transmission
Transmission measurements were completed with a Perkin-Elmer Lambda 950 UV/Vis/NIR spectrometer with ITO coated substrates as references.

1.3.6. Wetting Characterizations
The contact angle measurements were measured with a positioning stage, dosing needle and a Nikon D5200 with a macroscopic lens and analysed with Image J software as described by Stalder et al.[4]

1.3.7. GIWAXS
Grazing Incidence Wide Angle X-ray Scattering (GIWAXS) measurements were conducted at PLS-II 9A U-SAXS beamline of Pohang Accelerator Laboratory (PAL) in Korea. The X-rays from the vacuum undulator (IVU) were monochromated using Si(111) double crystals

and focused on the detector using K-B type mirrors. Patterns were recorded with a 2D CCD detector (Rayonix SX165). The sample-to-detector distance was about 225 mm for energy of 11.08 keV (1.119 Å).

1.3.8. Spectroscopic Ellipsometry

Spectroscopic Ellipsometer (SE from Ellipso technology Co., Inc.) was used in the measurement of the rotating polarizer type. The spectroscopic ellipsometry measurements were performed in the spectral range of 1.2-5.2 eV (~ 240-1000 nm) for three angles of incidence ranging from 60° to 70° with a 5° step. This approach improves the accuracy of the calculations allowing the determination of film thicknesses and optical refractive index values. The measured ellipsometric angles Ψ and Δ are defined from the ratio of the reflection coefficients r_p and r_s for the p- and s- polarizations, respectively, (i.e., polarization of the electric field parallel and perpendicular to the plane of incidence) according to

$$\frac{r_p}{r_s} = \tan\psi e^{i\Delta} \tag{6}$$

From the analysis of the SE measurement data, the dielectric function of a certain material is determined. For this, the optical response of the measured samples was modelled in the Tauc-Lorentz dispersion formula,[5] which included multiple oscillators.

$$\varepsilon_{i,TL}(E) = \varepsilon_{i,L} \times \varepsilon_{i,T} \tag{7}$$

$$\varepsilon_{i,TL}(E) = \frac{1}{E}\frac{AE_oC(E-E_g)^2}{(E-E_o)^2 + C^2E^2} \qquad \text{for } E > E_g$$

$$\varepsilon_{i,TL}(E) = 0 \qquad \text{for } E \leq E_g$$

$$\varepsilon_r(E) = \varepsilon_r(\infty) + \frac{2}{\pi}p\int_{E_g}^{\infty}\frac{\xi.\varepsilon_i(\xi)}{\xi^2 - E^2}d\xi \tag{8}$$

And the experimental ellipsometric data were fitted using the Levenberg-Marquardt algorithm for minimizing the mean-squared error (MSE).

$$MSE = \frac{1}{2N-M}\sum_{i=1}^{N}[(\alpha_i^{mod}-\alpha_i^{exp})^2 + (\beta_i^{mod}-\beta_i^{exp})^2] \tag{9}$$

where N is the number of (α, β) pairs, M is the number of fitted parameters in the model. The superscripts *mod* and *exp* indicate model-generated and experimental data, respectively.

### 1.3.9. Electric Field and Absorption Calculations

The invariant imbedding method is a powerful tool for handling the electromagnetic wave propagation in one-dimensional inhomogeneous media. The Maxwell's equations were applied to the amplitude of the electric field. The exact differential equations satisfied by the reflection coefficient and the electric field amplitude were obtained with respect to medium size. These were supplemented with the initial conditions from Fresnel formulas.[6,7] Using this method, we obtained the exact solutions for the reflection and transmission coefficients of incident waves and electric field amplitudes inside the organic photovoltaic (OPV) media.

## 2. Interfacial and Electronic Characterizations

2.1. Surface Morphology

The topography images were Fourier filtered to remove from the data the frequency components associated with very weak signal, and the frequency regime affected by electrical and mechanical noise. The images were then Fourier Transformed to obtain the 2D Power Spectrum Density (PSD) presented in Figure S1a-c. The 2D-PSD was then radially integrated to reflect the root mean squared (*RMS*) roughness of the sample surface. The resulting spectra confirmed that the fluorination had little impact on the PEDOT:PSS layer roughness, which as a consequence cannot be used to explain the variations of the device characteristics when fluorinating their HTLs.
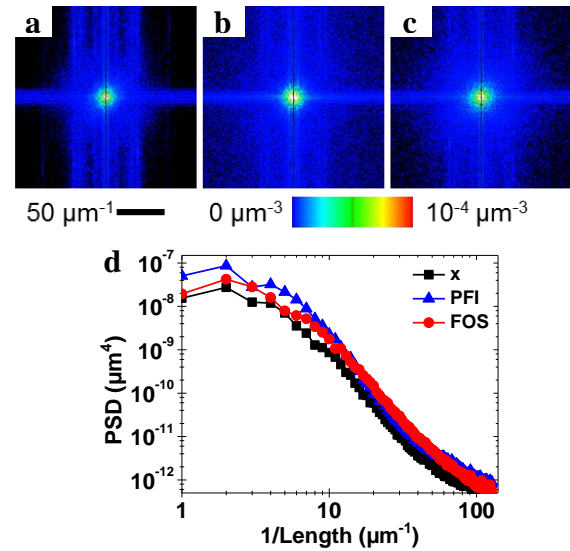
Figure S1. Fourier Transforms (FT) of AFM images. PEDOT:PSS based thin films: pristine **(a)**, mixed with PFI **(b)** and with FOS **(c)**. Radially integrated FTs (d) for PEDOT:PSS pristine (■), mixed with PFI (▲) or FOS (●).

2.2. Morphology-W_f Correlations

Figure S2 shows large scale representations of the surface potential map overlaid on top of the topography for each hole transport layer (HTL). Both set of data were recorded simultaneously. The largest average surface potential variation is observed when PFI is used as a fluorination agent.
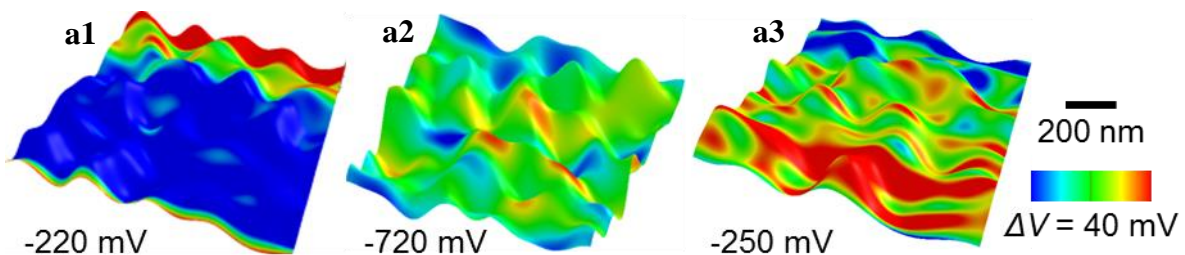

Figure S2. Surface potential on the topography of PEDOT:PSS thin films: pristine **(a)**, PFI- **(b)** and FOS-mixed **(c)**.

As discussed in the main manuscript, none of the sample presents any correlation between surface potential fluctuations and surface topography. This could be consistent with probing different orientations of the PEDOT crystalline grains distributed within the hole transport layer below the upper interface of the blend layer rich in PSS, PFI and FOS.

AFM measurements were also carried out in non-contact mode. The literature suggests the top of the PEDOT:PSS to be rich of insulating PSS, PFI and FOS.[8,9] In contrast, the present samples showed no noticeable potential variation contrast. This could be associated with a loss of resolution due to the Pt-coated Si tip required for KPFM acquisition.

2.3. UV Photoemission Spectroscopy

A discharge lamp provided an He I ($h\upsilon = 21.22$ eV) radiation with a resolution of 0.15 eV. The samples were transferred into the chamber one-by-one, and thin films were used to minimize the risk of charging. Charging and evolution of the samples when exposed the UV light source of the UPS were not observed. The UPS measurements of the photoemission onset were completed with a negative 5 V bias applied to the sample (Figure S3). Similar observations as those reported for the Kelvin probe measurements can be made with the ionization potential values deduced from the UPS measurements (Table S1). The discrepancies between the values obtained with these three different techniques are expected and ex plained by the different atmospheres and experimental conditions associated with each type of measurements, i.e ambient conditions, inert atmosphere and ultra-high vacuum for the Kelvin probe, the KPFM and UPS
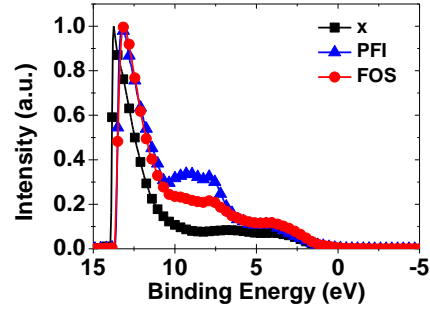

Figure S3. Normalised UPS spectra of PEDOT:PSS thin films spin-coated on quartz substrates: pristine (■), mixed with PFI (▲) and with FOS (●).

experiments, respectively.[10-14] In the case of the UPS measurements, a further contribution could arise from UV exposure.[15] These explain the value differences between the results provided by each technique.

Table S1. Ionization potential as deduced from UPS measurements (I_P) along with nanoscopic and macroscopic work functions ($W_{f\text{-}KPFM}$, $W_{f\text{-}mKP}$ in eV) from PEDOT:PSS based thin films.

Fluorination	x	PFI	FOS
I_P (eV)	5.19 ± 0.02	7.32 ± 0.02	7.09 ± 0.02
$W_{f\text{-}KPFM}$ (eV)	4.70 ± 0.02	5.40 ± 0.03	4.90 ± 0.03
$W_{f\text{-}mKP}$ (eV)	5.20 ± 0.02	5.72 ± 0.02	5.56 ± 0.02
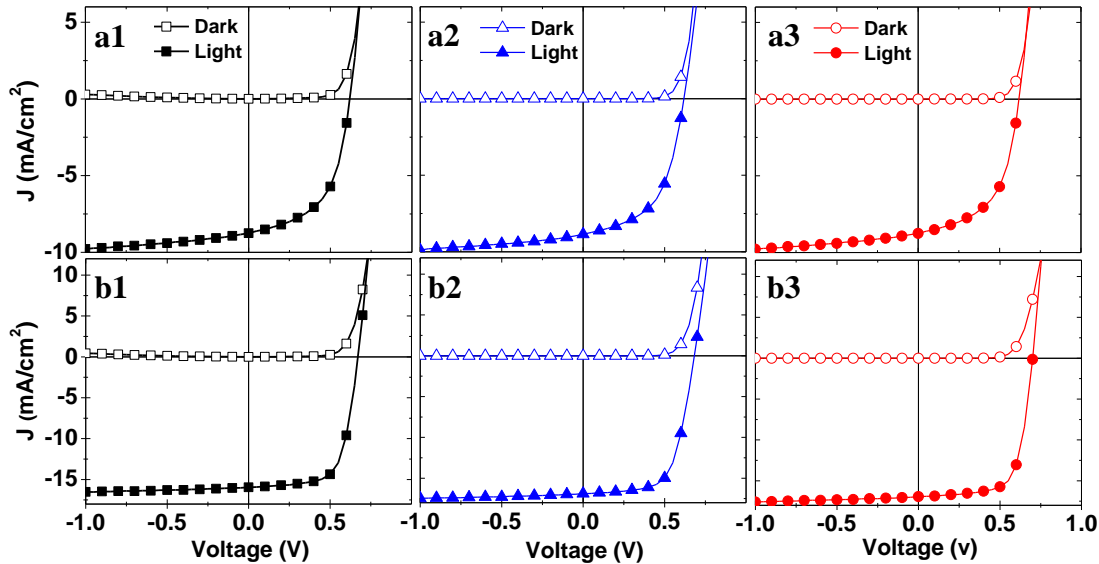
Figure S4. P3HT:PC$_{60}$BM (**a**) and PTB7:PC$_{70}$BM (**b**) solar cells using PEDOT:PSS (**1**, ■), PEDOT:PSS:PFI (**2**, ▲), and PEDOT:PSS:FOS (**3**, ●) as the hole transport layer. Empty and filled symbols (square, triangle, disk) stand for dark and illuminated conditions, respectively.

3. Solar Cell Analysis
3.1. J$_{sc}$ and EQE Consistency

Using an AM1.5G spectrum from NREL and the *EQE* data, J_{SC}-*EQE* could be calculated and compared with J_{SC} direct measurements. The values are presented in Table S2 and illustrate the good agreement between *EQE* and *J-V*.

3.2. Dark J-V Characterizations

For comparison purposes, Figure S4 presents the *J-V* curves in the dark and under 1.0 Sun illumination.

3.3. Series and Shunt Resistances

In first approximation,[16] the single diode model solar cell was used to extract series resistance, r_s, and shunt resistance, R_{sh}, values which are presented in Table S2. r_s results from the charge displacement across the materials and the contacts between the active material and the electrodes, which tend to reduce the fill factor of the device. The value of r_s was estimated by calculating the slope of the *V-J* curve at V_{OC}. Within the precision of the approach the assessed values of r_s remains relatively

unchanged for both PTB7:PC$_{70}$BM and P3HT:PC$_{60}$BM devices, despite the slight increase of V_{OC} and *FF* reported in Table 3 of the main manuscript. This comes in contrast with the decreased r_s values observed for instance in organic-inorganic Schottky solar cells,[17] and suggests that in the present more complex systems a 1st approximation model is not sufficient to describe the current flow across the device and its interfaces when using fluorinated PEDOT:PSS.

Table S2. Short circuit current density (J_{SC}), external quantum efficiencies integrated over the 300-800 nm spectral range ($S_{EQE,\lambda}$) and J_{SC} calculated from the *EQE* data (J_{SC-EQE}); series (r_s) and shunt (R_{sh}) resistances extracted from the the *J-V* curves.

	Fluorination	x	PFI	FOS
P3HT:PC$_{60}$BM	J_{SC} (mA/cm^2)	8.842	8.855	8.628
	$S_{EQE,\lambda}$ (k%.nm)	14.7	15.2	14.7
	J_{SC-EQE} (mA/cm^2)	7.92	8.21	7.85
	r_s (Ω.cm^2)	15	17	15
	R_{sh} (kΩ.cm^2)	0.5	0.5	0.4
PTB7:PC$_{70}$BM	J_{SC} (mA/cm^2)	15.944	16.889	16.941
	$S_{EQE,\lambda}$ (k%.nm)	28.3	29.6	30.2
	J_{SC-EQE} (mA/cm^2)	16.15	16.62	16.96
	r_s (Ω.cm^2)	7	7	5
	R_{sh} (kΩ.cm^2)	1.3	1.1	0.9

R_{sh} is thought to be mostly due to defects associated with alternative current pathways within the active media. Its effect is considered most important at low illumination and at low voltages. The value of R_{sh} was estimated by calculating dV/dJ at 0 V, leading to values which also remains relatively unchanged with the fluorination in the case of P3HT:PC$_{60}$BM devices, or would appear to decrease slightly in the case of PTB7:PC$_{70}$BM devices. The apparent discrepancy between PCE-V_{OC}-FF and r_s-R_{sh} values suggests that more accurate device modeling would be needed to extract more reliable r_s and R_{sh} values. Considering the dark *J-V* curves (Figure S4) led to R_{sh} values,[18] which were also deemed unreliable within the experimental precision. Multiple illumination intensity measurements and more complex modelling might overcome this situation,[16,19] however, due to the complexity of the systems herein presented, these approaches fall beyond the scope of this manuscript.

4. EQE Spectral Variations with HTL Fluorination

To understand the origin of the *EQE* spectral variations presented in Fig. 5a of the main manuscript, several hypotheses were explored. These include that the HTL fluorination could
a) change the HTL transmission spectra,
b) alter the surface energy at the HTL polymer:PCBM blend interface. By doing so, the blend morphology could be impacted as discussed in the main manuscript based on the literature.[20-38] This should be associated with changes in the absorption spectra of the blend as well as crystallinity, orientation, domain size and/or

polymer:PCBM profile.
c) alter the thickness or change the absorption coefficient of the device layers, which either of them would impact on the electro-optical properties of the devices.
In this section, we then start to analyze the differential EQE variations and address each of the above hypotheses.

4.1. Active Layer Optical Density Variations
The relative variations of the *EQE* data are presented in Figure S5 using pristine PEDOT:PSS based devices as a reference. The *EQE* values obtained with P3HT:PC$_{60}$BM OPVs display weaker variations than those obtained with PTB7:PC$_{70}$BM devices, Figure S5a and b respectively, but both show a noticeable dependence with the excitation wavelength.
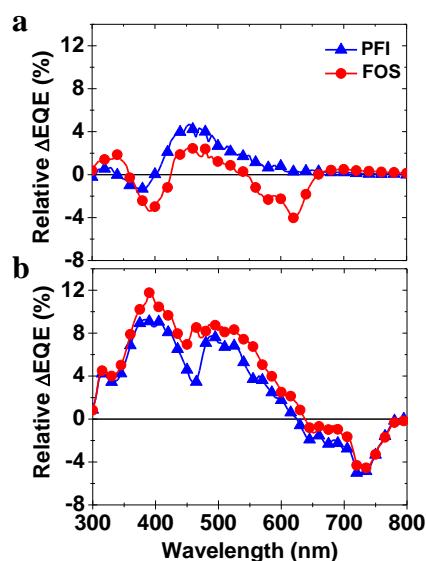
Figure S5. Relative *EQE* spectral variation for P3HT:PC$_{60}$BM **(a)** and PTB7:PC$_{70}$BM **(b)** with pristine PEDOT:PSS based devices used as a reference for PFI ($\blacktriangle$) and FOS ($\bullet$) mixed hole transport layer.

4.2. HTL Optical Transmission
Figure S6 presents the transmittance spectra of fluorinated and pristine PEDOT:PSS thin films. It is obvious from the amplitude of the variation, i.e. less than 3 %, as well as the absence of spectral deviation that the fluorination does not alter enough the photophysical properties of the hole transport layer to explain the *EQE* spectral variation reported in Fig. 5 of the main manuscript for both P3HT and PTB7 based OPVs. In addition, we note that the *EQE* of both P3HT and PTB7 based devices are not affected in the same manner as illustrated in Figure S5. As a conse-
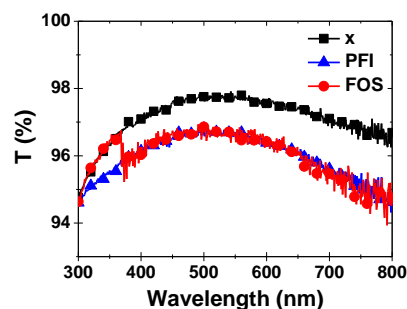

Figure S6. Transmittance spectra of PEDOT:PSS thin films spin-coated on quartz substrates: pristine ($\blacksquare$), mixed with PFI ($\blacktriangle$) and with FOS ($\bullet$).

quence, the absorption of the fluorinated PEDOT:PSS can be definitely ruled out (hypothesis a) and other origins have to be investigated. In this context, the variation of the surface energy when fluorinating the HTL was quantified by contact angle measurements on ITO and on the PEDOT:PSS based thin films.

4.3. Wetting Properties

Figure S7 illustrates the variation of the contact angle associated with the fluorination of PEDOT:PSS. Variations of the contact angles are visible for both PEDOT:PSS on quartz substrates, Figure S7a, and dichlorobenzene on the HTL thin films, Figure S7b. The contact angle values are listed in Table S3.
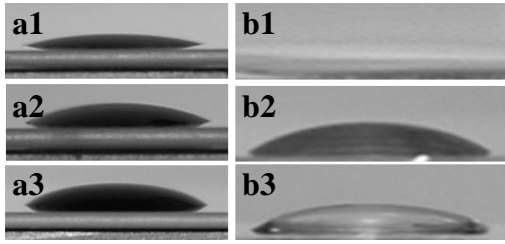
Figure S7. Contact angle measurements of PEDOT:PSS on quartz substrates (**a**) and of dichlorobenzene on PEDOT:PSS based thin films (**b**): pristine (**1**), mixed with PFI (**2**) and with FOS (**3**).

From the Young and Dupré equations, eq. 10 and 11 respectively,[4] we obtain eq. 12 from which the adhesion energy of the dichlorobenzene on the PEDOT:PSS based surfaces can be assessed.

$$\gamma_{SV} = \gamma_{SL} + \gamma_{LV} \cos\theta_c \qquad (10)$$

$$E_{adh} = \gamma_{SV} + \gamma_{LV} - \gamma_{SL} \qquad (11)$$

$$E_{adh} = \gamma_{LV}(1 + \cos\theta_c) \qquad (12)$$

with γ_{SV}, γ_{SL}, γ_{LV} being the solid-vapor, solid-liquid and liquid-vapor interfacial tensions, respectively. θ_c is the equilibrium contact angle that the drop makes with the surface and E_{adh} is the adhesion energy defined as the amount of energy involved to separate the liquid from the surface. γ_{LV} is taken as the dichlorobenzene surface tension, which value is 26.84 mN/m at 25 °C.

Table S3. Contact angle (θ_c) variation with PEDOT:PSS fluorination in two distinct configurations and adhesion energy, E_{adh}, calculated with eq. 12.

Interface	Solution	θ_c (°) / E_{adh} (mN/m)	Picture
glass	PEDOT:PSS	11.6 / --	a1
glass	PEDOT:PSS:PFI	21.2 / --	b1
glass	PEDOT:PSS:FOS	37.7 / --	c1
PEDOT:PSS	Dichlorobenzene	2.6 / 53.7	a2
PEDOT:PSS:PFI	Dichlorobenzene	38.1 / 48.0	b2
PEDOT:PSS:FOS	Dichlorobenzene	47.8 / 44.9	c2

The calculated values the adhesion energy are listed in Table S3. There is a moderate but clear decrease of the surface energy with the PEDOT:PSS layer fluorination. Noticeably, the variation of the surface energy herein reported is nonetheless weaker than reported in the literature, as for instance when PEDOT:PSS, SiO$_2$ and poly(thienothiophene):Nafion were used.[39]

4.4. Polymer:PCBM Blend Optical Absorbance

To focus on the photo-active blend displaying the largest *EQE* amplitude variations, the relative absorbance of each PTB7:PC$_{70}$BM device is reported in Figure S8. Its variation turned out to be measureable but nonetheless relatively moderate, i.e. < 6 %. Compared to the PEDOT:PSS based devices, the fluorinated HTL devices do display an increased absorbance which, within the experimental precision, could be consistent with the *EQE* spectral variation (Figure S5b vs Figure S8). The variation of the PTB7:PC$_{70}$BM absorption coefficient herein reported could be seen as consistent with the surface energy of the fluorinated PEDOT:PSS layer which could influence the PTB7 structure at the interface of the hole transport layer.
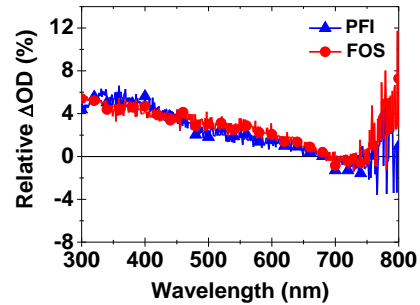
Figure S8. Relative OD variation for PTB7:PC$_{70}$BM with pristine PEDOT:PSS based devices used as a reference for PFI (▲) and FOS (●) based HTL.

On the one hand, we note that PTB7 has been found to display an ordered fraction as small as fraction 20 %.[40] As a consequence, this rather small ordered fraction could leave room for a relatively strong effect of the substrate surface energy on PTB7 based photoactive blends. In contrast, annealed P3HT is known to be rather crystalline, and the *PCE* increase upon PEDOT:PSS fluorination was more modest than for PTB7 devices. This could be consistent with the fact that we could not observe any variation of the absorbance larger than the experimental uncertainty.

On the other hand, we note a potential inconsistency in the fact that P3HT:PC$_{60}$BM does not present any obvious change of absorption, not even around 620 nm, which is associated to this polymer crystallization. Along similar lines of thoughts, P3HT:PC$_{60}$BM displays its strongest *EQE* relative variations in the UV range and not around 620 nm, Figure S5a.

Consequently and despite the contact angle data, the absorption results do not unambiguously support the hypothesis that the morphology, i.e. the crystallization, of the active layer would be altered by the fluorination of the PEDOT:PSS layer. To address this ambiguity, GIWAXS measurements were undertaken.

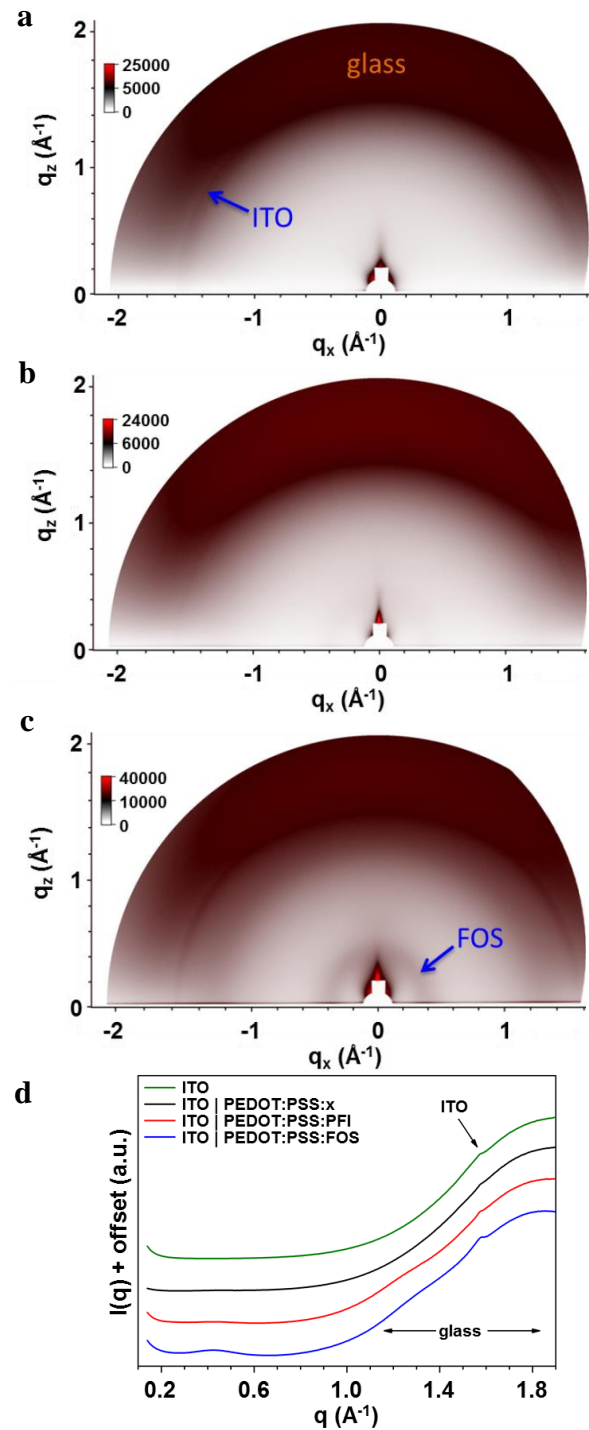### 4.5. GIWAXS
4.5.1. Neat and Fluorinated PEDOT:PSS
As illustrated in Figure S9, the GIWAXS patterns of PEDOT:PSS films spincoated on top of a silicon wafer contain two broad continuous rings at roughly 1.2 and 1.8 Å^{-1}, whose location and width are in good agreement with the previously described nanocrystalline structure.[41] The fluorination expectedly preserves the rings and the nanocrystals, as the fluorinated alkyl (FA) chains are not miscible with the PEDOT:PSS segments. Patterns should therefore contain a specific signal from domains of close-packed FA chains, thus a scattering maximum around 1.15
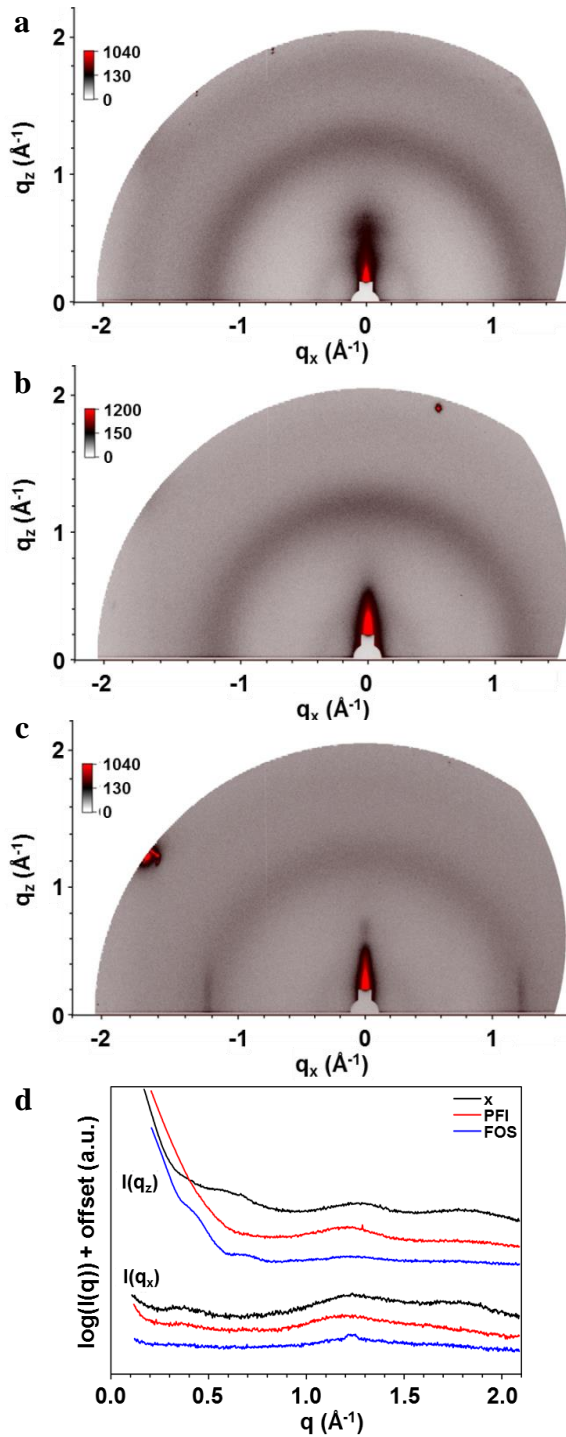
Figure S9. GIWAXS patterns with an incident angle α_i = 0.13° for pristine **(a)**, PFI- **(b)** and FOS- **(c)** mixed PEDOT-PSS layers deposited on silicon substrate. Profiles extracted from the GIWAXS patterns **(d)**.

Figure S10. GIWAXS patterns with α_i = 0.13° of ITO substrate, bare **(a)** and covered with neat **(b)** or FOS-based **(c)** PEDOT-PSS, (α_i = 0.13) and profiles **(d)** within Ψ = -30° to -60° sector (origin on the meridian). The wide-angle region is dominated by the scattering of the glass substrate. Only the contribution of molecular FOS layers (scattering maximum: D_{FOS} = 15 Å; $\xi \approx$ 30 Å) needs to be considered in the small-angle region.

Å^{-1} in the molten state or a sharp first order reflection at about 1.20 Å^{-1} for a long-range correlated hexagonal in-plane arrangement.[42]

The ramified architecture of PFI favors the short-range correlated organization, which gives rise to a diffuse signal overlapping the PEDOT:PSS ring. Both contributions were thus not separable for PFI, contrarily to FOS, for which a sharp elongated spot at 1.20 Å^{-1} is clearly observed on the equator and evidences crystallized FA chains layers lying parallel to the film surface.

As the organic semiconductor morphology often depends on the preparation conditions, films investigated by GIWAXS were also deposited under experimental conditions as close as possible to those used to fabricate the devices. This includes the use of ITO glass substrates, which however renders the wide-angle region unusable,

due to its own intense scattering. This is illustrated in Figure S10 for bare ITO substrate (a), as well as pristine (b) and FOS (c) -based PEDOT:PSS thin films.

4.5.2. P3HT based Bilayers

Regarding P3HT samples, the organic semiconductor molecules self-organize in crystalline lamellae formed by alternating rows of π-stacked backbones and aliphatic layers. The GIWAXS pattern of P3HT deposited on top of PEDOT:PSS itself covering a silicon wafer is presented in Figure S11a.
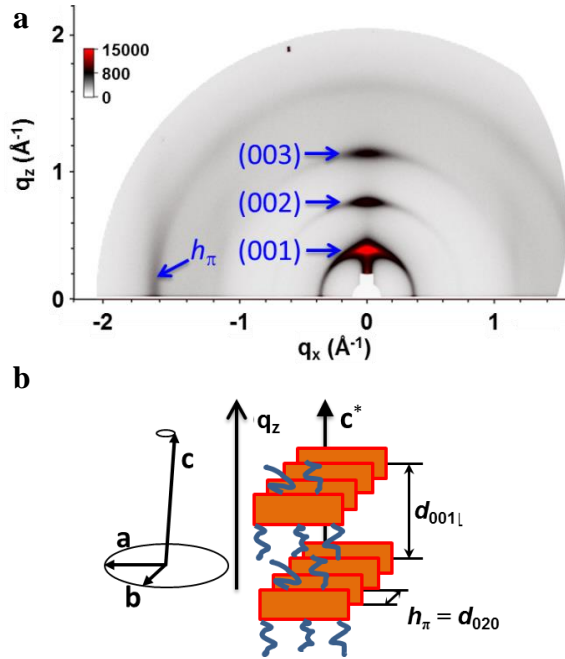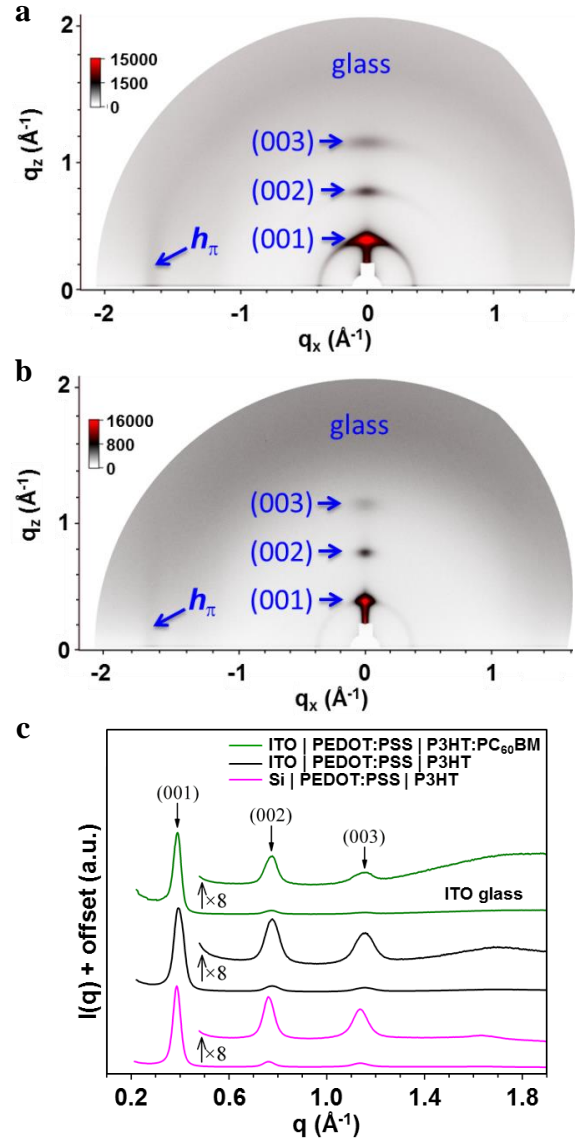

Figure S11. P3HT on top of neat PEDOT-PSS deposited on a silicon wafer: GIWAXS pattern with an incident angle $\alpha_i = 0.12°$ **(a)**, schematics of the polymer domains with short-range correlated structure and orientation **(b)**.

Only signals from P3HT remain therefore visible with the main signals being composed by a series of sharp harmonics from a 17 Å periodicity (first order at ca. 0.37 $Å^{-1}$) and a somewhat broadened signal at 3.8 Å (ca. 1.65 $Å^{-1}$). In agreement with structural studies on bulk P3HT powder pattern, the latter signal corresponds to the stacking distance, h_π, between π-stacked backbones, while the set of (00l) reflections comes from lamellae formed by alternating polythiophene sublayers and alkyl chains. The (00l) reflections group lies on the meridian while h_π lies on the equator, which proves that P3HT is a mosaic texture of flat lying lamellae. This lamellar crystalline structure and the preferential flat-on alignment of the lamellae is illustrated schematically in Figure S11b. This orientation and the spacing values are in agreement with alignments and lattice parameters previously reported for P3HT thin films (a = 7.8 Å, b = 2h_p = 7.8 Å, c = 16.0 Å, γ = 93.5°).[43]

The same morphology is found for the P3HT films deposited on top of PEDOT:PSS spincoated on ITO-glass and silicon wafer substrates. In particular, P3HT shows the same flat-on alignment of crystalline lamellae (Figure S12a and Figure S11a). This also demonstrate that this morphology is not altered by the presence of the PEDOT:PSS bottom layer, which is slightly different from the observations made with PTB7 in the following section.

This orientation of the P3HT domains is maintained in the $PC_{60}BM$ blends (Figure S12b) with nearly the same parameters and an even further improved flat-on alignment of the lamellae, as discussed below.

Figure S12. GIWAXS patterns of neat P3HT **(a)** and P3HT:PC_{60}BM blend **(b)** films on top of neat PEDOT:PSS spincoated on ITO substrates (α_i = 0.13°). $I(q)$ profiles within Ψ = -3° to +3° sector (origin on the meridian) of the GIWAXS patterns (a), (b) and Figure S11a **(c)**.

Both P3HT and P3HT:PC_{60}BM were also deposited on top of neat, and fluorinated PEDOT:PSS. No influence of the HTL fluorination could be evidenced, even if several incident angle and thus weighting of the successive P3HT film strata were investigated as illustrated in Figure S13a. Comparing Figure S13b1 and b2 reveals the further improved flat-on alignment of the lamellae when PC_{60}BM is blended with P3HT. This is demonstrated by the decrease of the full widths at half maximum of the (001) spot, from $\Psi_{FWHM} \approx$ 14-20° to ca. 7°, with the addition of PC_{60}BM. Finally and in a similar manner as what will be seen in the following section with the PTB7 system, P3HT domains are slightly but significantly modified by the blending with PC_{60}BM. In this case the thickness and the correlation length of lamellae are d = 16.3 ± 0.1 Å and $\xi \approx$ 150 Å in the blends, instead of 16.1 ± 0.1 Å and $\xi \approx$ 120 Å
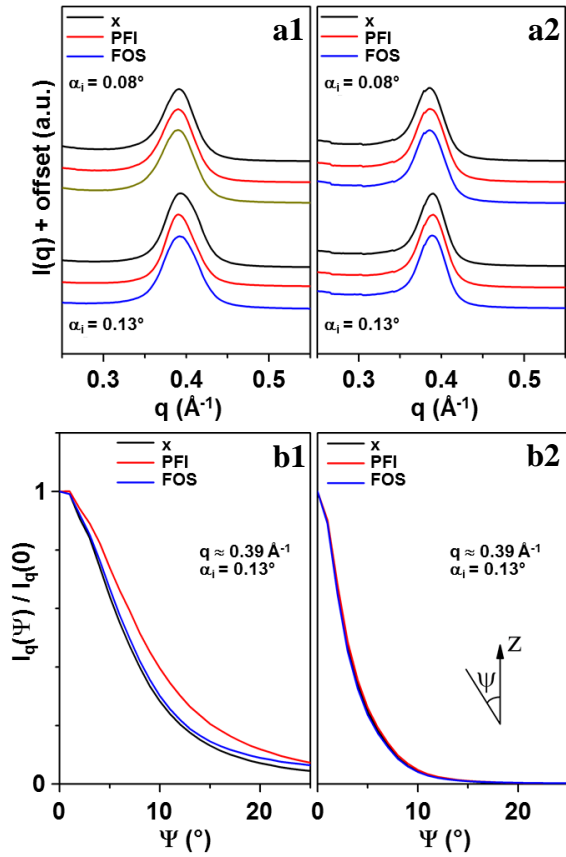
Figure S13. $I_0(q)$ profiles patterns (**a**) and normalised $I_q(\Psi)$ ring profiles (**b**) of GIWAXS of neat P3HT (**1**) and P3HT:PC$_{60}$BM blend (**2**) thin films on top of pristine and fluorinated PEDOT:PSS layers. Sector profiles (**a**) are plotted with an offset to facilitate the comparison of shapes and maximums [sector from Ψ = -3° to +3° and incident angles α_i = 0.08° (top) and α_i = 0.13° (bottom)], while azimuthal profile intensities (**b**) are normalized to the maximum $I_q(0)$ on the meridian [$I_q(\Psi)$, q = 0.392 Å^{-1}; width: D_q = 0.040 Å^{-1}].

in pristine P3HT films. Noticeably, these features, i.e. ξ and Ψ_{FWHM}, variation with the insertion of PC$_{60}$BM, were observed for both fluorinated and pristine PEDOT:PSS bottom layers.

4.5.3. PTB7 based Bilayers

When silicon substrates are used for PTB7 film deposition, all the characteristic signals of the structure are visible and shown in Figure S14a. They correspond to two broad and intense structure peaks around 0.35 Å^{-1} and 1.3-1.5 Å^{-1}:

- the wide-angle ring arises from the lateral distances between irregularly piled backbones, h_π, and between aliphatic chains, h_{ch},
- the two semi-diffuse small-angle rings labeled as (1) and (2) in Figure S14a result from alternativing backbone rows and aliphatic layers, d_1 and second order periodicity d_2.

These features are schematically represented in Figure S14b. Noticeably, these rings are nearly isotropic and exclude any significant alignment of the short-range correlated lamellae. As discussed below, this comes in contrast with the preferential orientations reported in literature.[40,44,45]

PTB7 is known to self-organize in a short range correlated structure formed by alternative rows of irregularly face-to-
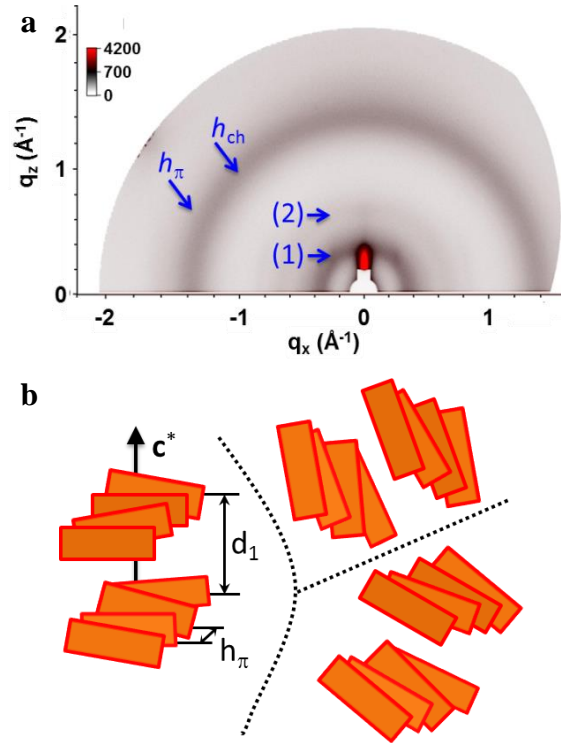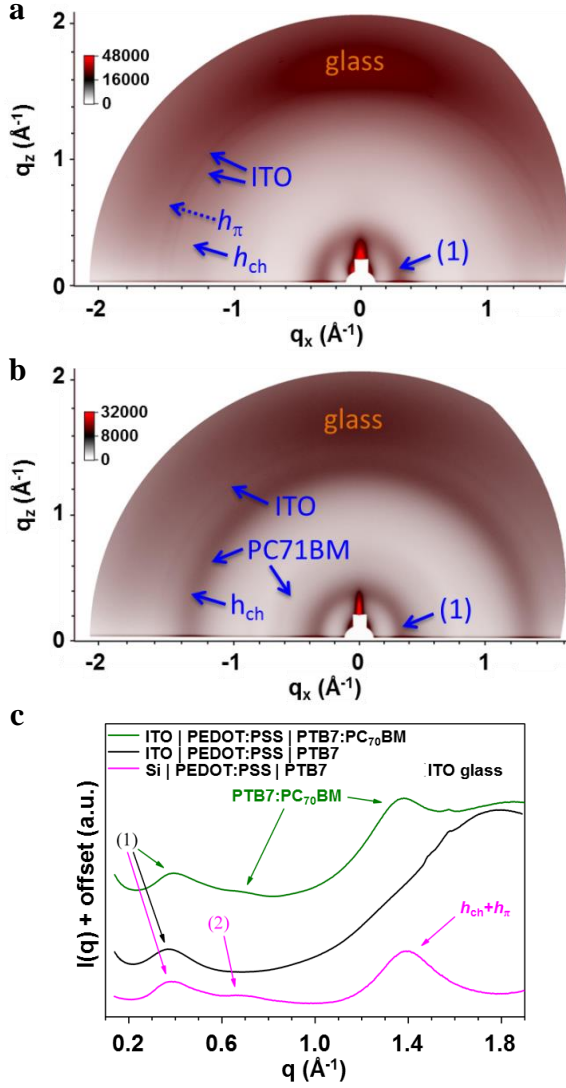

Figure S14. PTB7 on top of neat PEDOT-PSS deposited on a silicon wafer: GIWAXS pattern with an incident angle α_i = 0.12° (**a**), schematics of the polymer domains with short-range correlated structure and variable orientations (**b**).

face piled backbones and of aliphatic layers. The direction of alternation therefore designs a lamellar-like periodicity, $d_1 \approx 17$ Å, with in-plane periodicities overlapping contributions of lateral distances between molten aliphatic chains $h_{ch} \approx 4.5$ Å and piling distances of backbones $h_p \approx 3.9$ Å.[40] Roughly, the same structural parameters are found here for PTB7 deposited on top of PEDOT-PSS covered Si wafer. However no significant orientation can be recognized in the present study.

The literature reported a slight flat-on preferential orientation of lamellae for PTB7 films directly deposited on top of silicon.[40] Other references even reported more developed flat-on preferential alignment and slightly different structural parameters ($d \approx 20$ Å; $h_p \approx 4.2$ Å).[44] However, the apparent inconsistency probably comes from the absence of bottom layer in these references, since the PEDOT:PSS deposited herein expectedly modifies the anchoring of the PTB7 top layer.

The comparison of Figure S14a with Figure S15a illustrates that the use of ITO glass substrates did preserve the small-angle lamellar ring of PTB7 related to the alternation of alkyl-chains and conjugated moieties, while rendering the wide-angle region unusable due to the ITO glass intense scattering hiding the contributions from lateral spacing of alkyl chains and backbones. More specifically, the position of the maximum and the width of the lamellar first order rings appear to be the same regardless of the substrate while the intensity is quite homogenously distributed along the ring in both cases. The substitution of substrates did not change the organization but confirmed the absence of preferential orientations of lamellae, whether the films are constituted by neat PTB7 or PTB7:PC$_{70}$BM blend (Figure S15a and

Figure S15. GIWAXS patterns of neat PTB7 **(a)** and PTB7:PC$_{70}$BM blend **(b)** films on top of neat PEDOT-PSS spincoated on ITO substrates ($\alpha_i = 0.13°$). $I(q)$ profiles within $\Psi = -30°$ to $-60°$ sector **(c)** of the GIWAXS patterns (a), (b) and Figure S14a.

b). Figure S15b and c display the additional rings from PC$_{70}$BM domains, which have no strong effect on the PTB7 fraction, as its scattering rings remain similar to those observed in neat PTB7 films. As the films were spincoated on top of pristine and fluorinated HTLs, accurate information was extracted from sector profiles, excluding the distorted meridian and equatorial zones, and from ring profiles, which are presented in Figure S16a and b, respectively. The morphology of PTB7 (Figure S16a1-b1) and PTB7:PC$_{70}$BM (Figure S16a2-b2) films is independent of the fluorination of the PEDOT:PSS bottom layer. In particular the same lamellar periodicity and correlation length were identified among almost randomly oriented domains (Figure S14b). Moreover, the variation of incident angle, α_i, used to probe the films revealed that the lamellar ring were unchanged (Figure S16a). This shows that there are no substantial morphology changes across the thickness of the films. The only relatively significant difference between profiles is the somewhat smaller lamellar periodicity found for PTB7:PC$_{70}$BM blends ($d = 16.2 \pm0.2$ Å; $\xi \approx 30$ Å), when compared to neat PTB7 ($d = 17.1 \pm 0.2$ Å; $\xi \approx 30$ Å), presumably in
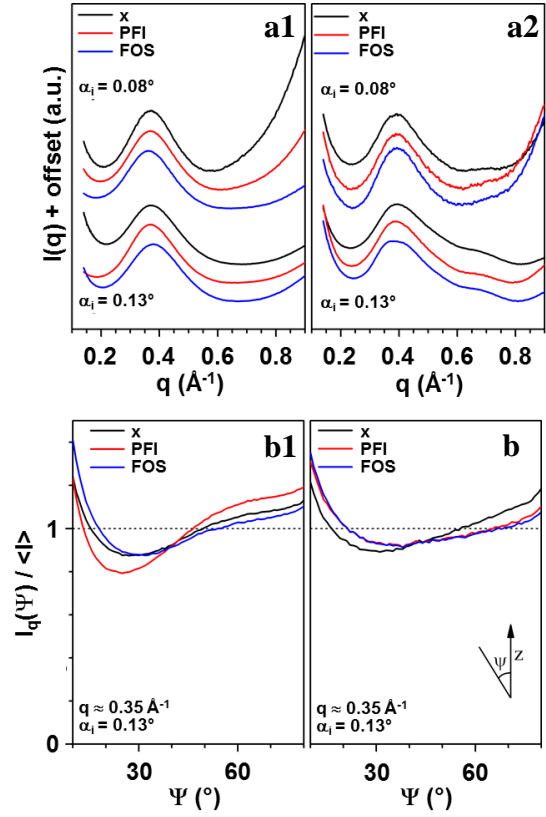
Figure S16. $I(q)$ profiles **(a)** and normalized $I_q(\Psi)$ ring profiles **(b)** of GIWAXS patterns of neat PTB7 **(1)** and PTB7:PC$_{70}$BM blend **(2)** thin films on top of fluorinated and pristine PEDOT:PSS layers. Sector profiles are plotted with an offset to facilitate the comparison of shapes and maximums [sector from $\Psi = -30°$ to $-60°$ and incident angles $\alpha_i = 0.08°$ (top) and $\alpha_i = 0.13°$ (bottom)], while azimuthal profile intensities are normalized to the average scattered intensity $\langle I_q \rangle$ (dotted line) [$I_q(\Psi)$, $q = 0.349$ Å^{-1}; width: $D_q = 0.060$ Å^{-1}].

relation with the incorporation of a small fraction of PC$_{70}$BM in the PTB7 domains. Noticeably, this slightly reduced spacing in the blend with respect to neat PTB7 was observed for both fluorinated and pristine PEDOT:PSS bottom layers.

4.5.4. Overall Effect of the HTL Fluorination on P3HT and PTB7 based Blend Morphology

Overall, with Figure S13 and Figure S16, this GIWAXS investigation shows that the fluorination of the HTL did not induce any detectable morphology variation of the blends. Even though local structural changes at the very interfaces remain possible, the absence of detectable influence of the HTL fluorination was observed for both P3HT:PC$_{60}$BM and PTB7:PC$_{70}$BM thin films, while the angle dependent GIWAXS measurements did not evidence any change of conjugated polymers and PCBMs concentration. The present findings are in contrast with what had been suggested in other reports considering the effect of PEDOT:PSS surface energy not complemented with morphology study.[37] We note however that the present HTL fluorination study differs from earlier studies having for instance studied P3HT and PCBM profile distribution on top of pristine PEDOT:PSS, plain SiO$_2$ and pristine PTT:Nafion, which present a much larger surface energy variation, from 23 to 72 mN/m^2, and which were probed by Near-Edge X-ray Absorption Fine Structure

(NEXAFS) spectroscopy.[39,46] In the latter study,[39] a single angle was used for Grazing incidence X-ray Diffraction characterization and no significant difference in the degree of crystalline order or crystal orientation was observed with different surface energy. Different P3HT:PCBM profile nonetheless suggested based on the models used by the authors to analyze ellipsometry and NEXAFS data. Our GIWAXS investigation did not reveal such a profile variation, which could be due to the relatively moderate surface energy variation induced herein by the fluorination of the HTL. It certainly underlines the importance of such GIWAXS measurements to directly probe the films morphology of bulk-heterojunction in the same conditions as those used to fabricate OPV devices.

To summarize, in both P3HT and PTB7 cases, the fluorination of the HTL layer improved the device performances, while the structure and the alignment of the polymers were shown to remain unaffected. These results exclude the hypothesis b) formulated at the beginning of the section 4. It is then safe to conclude that, in the present study, the effect of the HTL fluorination does not directly relate to the photoactive blend film morphology.

4.6. Dektak and Spectroscopic Ellipsometry
4.6.1. Thicknesses

The thicknesses of the multilayered structures have been measured by both dektak and spectroscopic ellipsometry,

Table S4. Thickness of the ITO, HTL and active layers involved in the devices and as measured by dektak and spectroscopic ellipsometry. Dimensionless parameter, z/L, indicating an interface between ITO, HTL, active layer and anode.

|	Fluorination	x	PFI	FOS
	d_{HTL}^{DekT} (nm)	34 ± 2 ‡	41 ± 3 ‡	39 ± 2 ‡
P3HT:PC$_{60}$BM	d_{Blend}^{DekT} (nm)	70 ± 7	58 ± 8	66 ± 9
	$d_{ITO}^{Ellip.}$ (nm)	131.4	132.8	134.2
	$d_{HTL}^{Ellip.}$ (nm)	61.0	65.6	64.5
	$d_{Blend}^{Ellip.}$ (nm)	60.1	62.2	59.7
	$z/L_{TTO\text{-}HTL}^{Ellip.}$	0.70	0.71	0.71
	$z/L_{HTL\text{-}Blend}^{Ellip.}$	0.57	0.57	0.57
	$z/L_{Blend\text{-}Anode}^{Ellip.}$	0.44	0.43	0.44
PTB7:PC$_{70}$BM	d_{Blend}^{DekT} (nm)	63 ± 6	63 ± 7	68 ± 8
	$d_{ITO}^{Ellip.}$ (nm)	134.3	134.5	133.6
	$d_{HTL}^{Ellip.}$ (nm)	60.0	63.4	64.2
	$d_{Blend}^{Ellip.}$ (nm)	54.1	55.7	59.2
	$z/L_{TTO\text{-}HTL}^{Ellip.}$	0.70	0.71	0.70
	$z/L_{HTL\text{-}Blend}^{Ellip.}$	0.57	0.57	0.56
	$z/L_{Blend\text{-}Anode}^{Ellip.}$	0.45	0.44	0.44

‡ measured as a single layer

and are summarized in Table S4. Within the experimental and fitting precision, the values obtained with the fluorinated HTL are marginally different for each technique. The average thickness of PEDOT:PSS given by dektak measurements increases by about 15 to 20 % with the fluorination which remain close to the total standard deviation of our measurements. The dektak thickness of the blends is obtained by subtracting the HTL layer from the total thickness of the bilayer. This incidentally increases the experimental uncertainty on the blend thickness, without leading to clear trend, as for instance PFI blends would be associated with a 7 % increase and a 5 % decrease of the P3HT:PC$_{60}$BM and PTB7:PC$_{70}$BM film thicknesses, respectively. Within the experimental and fit uncertainty, these thicknesses appear to be independent of the HTL fluorination. Ellipsometry data provided thicker HTL films by ~ 40 % when compared with dektak measurements, an apparent discrepancy which could be explained by both the pressure of the dektak tip on the soft organic HTL thin film and the model used to fit of the ellipsometry data.[47] However, when comparing the thicknesses obtained by ellipsometry for the same materials, the fluorination appears to induce a maximum of ~ 7 %, ~ 9 % and ~ 4 % variation on the HTL, PTB7:PC$_{70}$BM and P3HT:PC$_{60}$BM layer thicknesses, respectively. These variations are within the experimental and fit uncertainty, but also relatively small compared to controlled variation thickness variation reported in the literature which studied the effect of film thickness in OPVs.[48-54]

Overall and for each technique the variation of the blend thicknesses appear to be small compared with the spectral variation of the EQE, and consequently not to be the main parameter associated with the observed spectral changes of OPV efficiency. It is noticed that the lack of significant thickness variation excludes any change of mobility, which otherwise could have also altered the PCE.[55,56]

4.6.2. Optical Constants

The optical constants of each materials in all the device configurations were deduced from the spectroscopic ellipsometry data and are presented in Figure S17 for PEDOT:PSS and in Figure S18 for the photoactive layers of the devices.

Based on our GIWAXS data, the ellipsometry model considers homogeneous material distribution across each layer. PEDOT:PSS refractive index and extinction coefficient, (n, k), are consistent with the literature.[57-59] n and k also preserve the same general characteristics whether pristine or fluorinated HTL were prepared (Figure S17a). However, they also present a slight red shift and variation of amplitude of their main features, pristine is "bluer" and with larger amplitudes than FOS-mixed, while PFI-mixed PEDOT:PSS presents the most red shifted and smallest amplitude. We note that a progressive blue shift of the PEDOT:PSS features, i.e. band gap, could be observed when doped with DMF or de-doped with hydrazine vapors.[57,60] As a consequence, we associate the spectral red shift observed in the present study with the effect of the sulfonic acid groups of the fluorination agents on the PEDOT moieties and the electro-negative effect of the same fluorination agents. These are equivalent to negative Burstein shifts induced on the apparent band gap of semiconductor when extra charges are added, for instance, through doping.[61-64] We note that the trend on the amplitude of the extinction coefficient is consistent both with the known tendency of fluorinated materials to have a reduced refractive index compared to hydrogenated
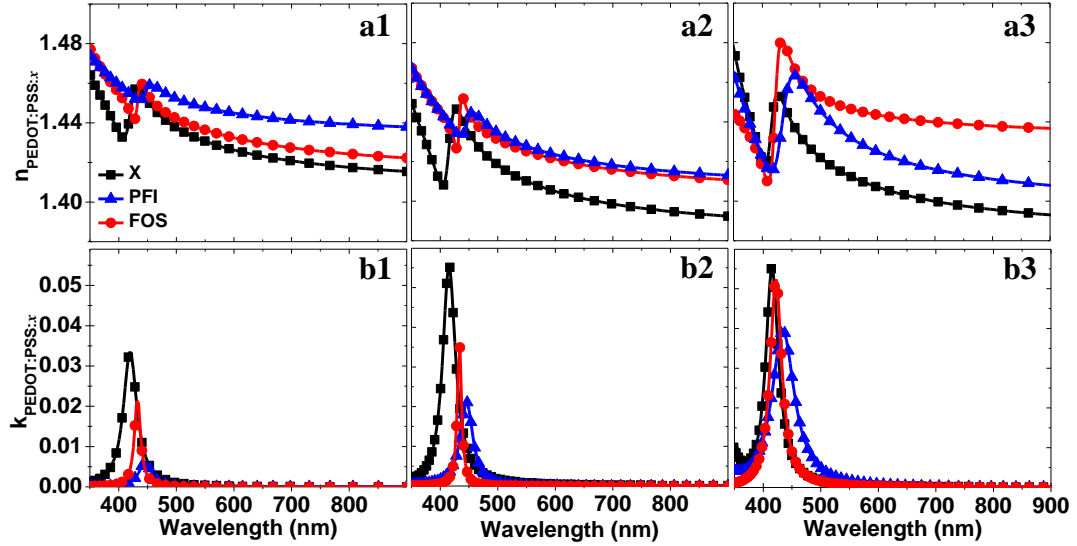
Figure S17. Refractive index, n (**a**), and extinction coefficient, k (**b**), of PEDOT:PSS pristine (■), mixed with PFI (▲) or FOS (●). HTL alone on top of ITO (**1**), HTL sandwiched between ITO and either P3HT:PC$_{60}$BM (**2**) or PTB7:PC$_{70}$BM (**3**).

counter parts,[65-72] and with the variation of n and k observed for various conjugated molecules in oxidized or reduced states.[73-75] This situation prevents any precise quantification of the relative contribution of these effects. As illustrated in Figure S17-2 and 3, the features evidenced with the fluorinated HTL single layers is qualitatively preserved once the PEDOT:PSS is covered by either P3HT:PC$_{60}$BM or PTB7: PC$_{70}$BM. However, we also note that the amplitude of the extinction coefficient is systematically increased once the HTL is coated by the blends. We associate this evolution with the dipoles formed due to the charge transfer between the blends and the PEDOT:PSS. Driven by the relative energy levels of of the compounds, as shown in Table 1 and Fig. 3 of the main manuscript, electrons are transfered from the blends to the PEDOT:PSS.

Figure S18 presents the optical constants of both P3HT:PC$_{60}$BM and PTB7:PC$_{70}$BM, which general features are in good agreement with the literature.[40,55,59,76] The extinction coefficients are also consistent with the

Figure S18. Refractive index, n (**a**), and extinction coefficient, k (**b**), of P3HT:PC$_{60}$BM (**1**) and PTB7:PC$_{70}$BM (**2**) on top of pristine (■), mixed with PFI (▲) or FOS (●) PEDOT:PSS spincoated on ITO susbstrates.

absorbance data presented in Figure S8 as well as Figure 3a1 and b1 in the main manuscript. This is obviously expected from the relation between α, the attenuation or absorption coefficient, k, the extinction coefficient, and λ, the wavelength.

$$\alpha = \frac{4\pi k}{\lambda} \tag{S13}$$

Slight variations of the optical constants of the blends with the HTL fluorination can be noticed. These variations, especially for P3HT:PC$_{60}$BM, appear weaker than those observed with PEDOT:PSS. In a similar manner as for this material, we associate the n and k variations to charge transfer across the HTL:blend interface.

4.7. Electro-Optical Modeling

The optical constants were used to model the modulus of the squared electric field, $|E|^2$, spectral distribution within the devices,[77] an approach which has been successfully used to optimize and explain the performances of OPV devices in both normal and reverse configurations.[48,78-80] $|E|^2$ for each device is presented in Figure S19. As commented in the main part of the manuscript, the HTL fluorination optical effect is revealed when $|E|^2$ colored map cross-sections, Figure S20a and Figure 8-1, are used to calculate the time average of the energy dissipated per second, Q.

For sake of simplicity we used $\tilde{Q} = n.k|E|^2/\lambda$ to compare the devices prepared with different HTL. In the case of P3HT:PC$_{60}$BM, we evidenced a marginal increase of $\tilde{Q}$ with PFI and FOS mixed PEDOT:PSS (Figure 8a2). This effect went up to 34 % increase of $\tilde{Q}$ in the case of PTB7:PC$_{70}$BM (Figure 8b2). With this stronger system, we then verified that a 20 % variation of the HTL thickness would not explain the EQE spectral variation. We considered the thickness of the pristine PEDOT:PSS layer as measured by ellipsometry and varied it by both ± 20 % (± 12 nm) to calculate $|E|^2$ and $\tilde{Q}$ as presented in Figure S20a and S20b, respectively. The $|E|^2$ curves present similar profiles, shifted with z/L, which is consistent with the thickness variation of the HTL layer. The maxima of $|E|^2$ located in the ITO is slightly increased for thinner HTL, while the maxima in the photoactive blends reach a similar amplitude. Figure S20b makes is easier to focus on what happens in the photoactive blends, where the $\tilde{Q}$ curves appear to present a similar amplitude
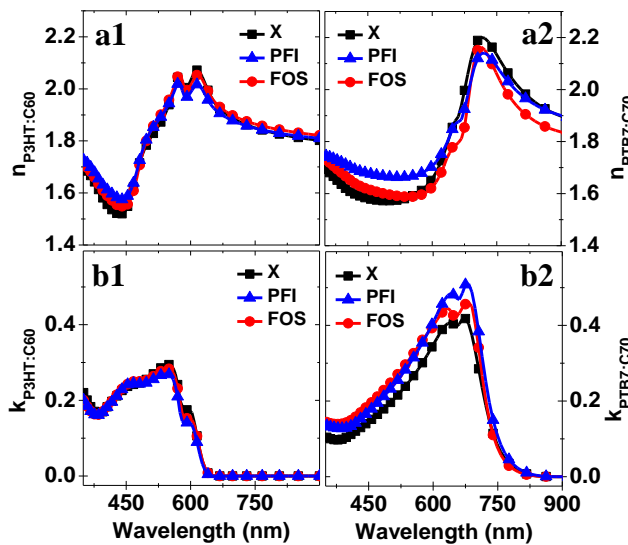
12/15
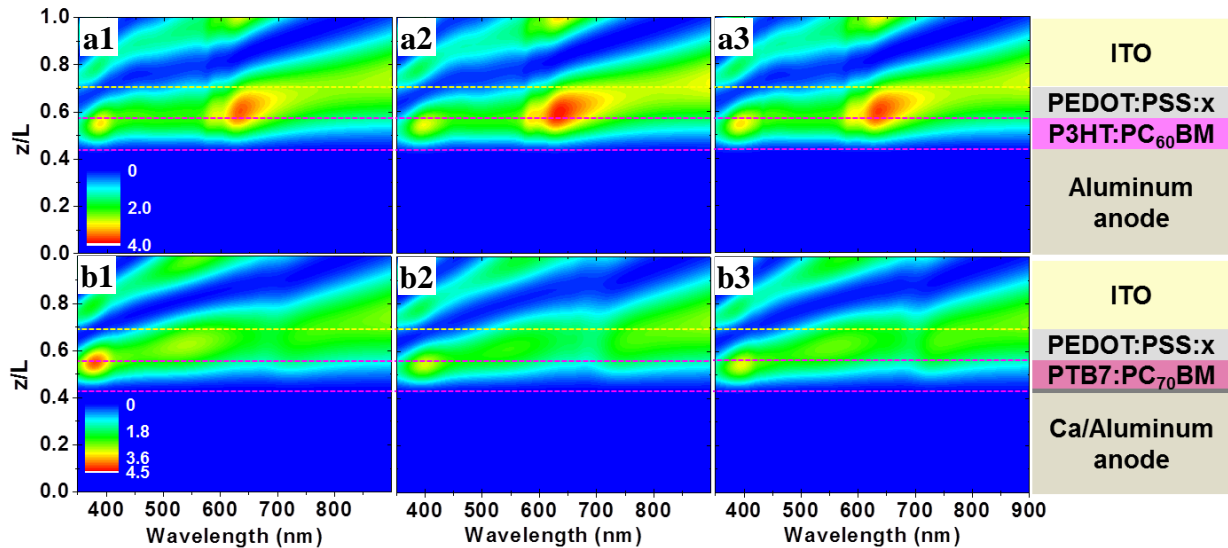
Figure S19. Calculated distribution of the modulus squared of the optical electric field, $|E|^2$, as a function of the incident wavelength inside the photovoltaics device made of P3HT:PC$_{60}$BM (**a**) and PTB7:PC$_{70}$BM (**b**) spincoated on top of pristine (**1**), PFI (**2**) and FOS (**3**) fluorinated-PEDOT:PSS. The horizontal dotted lines stand for the material distribution as labelled on the right hand-side.

regardless of the HTL thickness. To visualize any potential effect, we matched the position of the blend:anode interfaces. It is obvious in the insert of Figure S20b that the three $\tilde{Q}$ curves overlap. The integral of $\tilde{Q}$ over the z/L value corresponding to the PTB7:PC$_{70}$BM layer leads to a marginal variation of -5.4 % and +2.7 % compared to the device of the nominal HTL thickness. This is much lower than the effect of the fluorination on the optical constants.
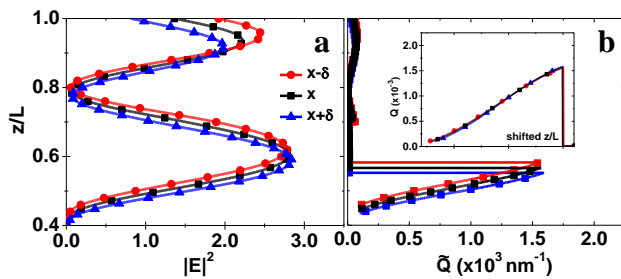
Figure S20. Distribution of $|E|^2$ (**a**) and calculated $\tilde{Q}$ values (**b**) across photovoltaic devices illuminated with a 500 nm monochromatic light, and made of PTB7:PC$_{70}$BM spincoated on top of pristine PEDOT:PSS films of nominal (■), -20 % (●) and +20 % (▲) thicknesses Insert: $\tilde{Q}$ values in the polymer:blend layers with z/L shifted to match the blend:anode interface.

5. Contributions

PA, KM and CTH discussed and initiated the project. PA organized, supervised and coordinated it. KM reviewed the literature, prepared most of the PEDOT:PSS based samples and prepared most figures of the manuscript, except those related to transient absorption, GIWAXS and electro-optical modelling. CTH prepared and characterized the devices in IDWS labs. CTH, KM and PA discussed and analyzed the data. HK and DWK were in charge of the near-field characterization, which was discussed with PA. TA was in charge of the macroscopic Kelvin probe measurements and organized the UPS measurements with AN completing and analyzing them. SF, JHK and JCR completed the conductivity measurements in CA lab. BH, SM and FM completed and analyzed the GIWAXS measurements, they also wrote the related section. KJL completed the transient absorption measurements in JWW lab and analyzed them with PA. KJL and SJK completed the

ellipsometry measurements, which were discussed with SYK, JWW and PA. SJK developed the ellipsometry models applied to the multilayer structure and KJL adjusted them to each system. EK completed some the dektak measurements. KJL developed the electrooptic modelling of the OPVs with PA's feedback. PA discussed each set of the data with their contributors and wrote the manuscript. The authors could comment the sections related to their contributions and provide general feedback.

6. References

1. D. A. Bonnell, *Scanning probe microscopy and spectroscopy : theory, techniques, and applications*, Wiley-VCH, New York, 2001.
2. A. Sohn, H. Kim, D.-W. Kim, C. Ko, S. Ramanathan, J. Park, G. Seo, B.-J. Kim, J.-H. Shin and H.-T. Kim, *Appl. Phys. Lett.*, 2012, **101**, 191605.
3. H. Kim, S. Hong and D.-W. Kim, *Appl. Phys. Lett.*, 2012, **100**, 022901.
4. A. F. Stalder, G. Kulik, D. Sage, L. Barbieri and P. Hoffmann, *Colloids Surf. A*, 2006, **286**, 92.
5. G. E. Jellison and F. A. Modine, *Appl. Phys. Lett.*, 1996, **69**, 371.
6. K. Kim, H. Lim and D.-H. Lee, *J. Korean Phys. Soc.*, 2001, **39**, L956.
7. K. J. Lee, J. W. Wu and K. Kim, *Opt Express*, 2013, **21**, 28817.
8. T. W. Lee, Y. Chung, O. Kwon and J. J. Park, *Adv. Funct. Mater.*, 2007, **17**, 390.
9. M.-R. Choi, T.-H. Han, K.-G. Lim, S.-H. Woo, D. H. Huh and T.-W. Lee, *Ang. Chem. Int. Ed.*, 2011, **123**, 6398.
10. R. Schlaf, H. Murata and Z. H. Kafafi, *J. Elec. Spectros. Rel. Phen.*, 2001, **120**, 149.
11. W. Gao and A. Kahn, *J. Appl. Phys.*, 2003, **94**, 359.
12. J. Hwang, A. Wan and A. Kahn, *Mat. Sci. Eng.*, 2009, **64**, 1.
13. Y. H. Zhou, C. Fuentes-Hernandez, J. Shim, J. Meyer, A. J. Giordano, H. Li, P. Winget, T. Papadopoulos, H. Cheun, J. Kim, M. Fenoll, A. Dindar, W. Haske, E. Najafabadi, T. M. Khan, H. Sojoudi, S. Barlow, S. Graham, J. L. Bredas, S. R. Marder, A. Kahn and B. Kippelen, *Science*, 2012, **336**, 327.
14. N. Koch, A. Vollmer and A. Elschner, *Appl. Phys. Lett.*, 2007, **90**, 043512.

15. Y. J. Lin, F. M. Yang, C. Y. Huang, W. Y. Chou, J. Chang and Y. C. Lien, *Appl. Phys. Lett.*, 2007, **91**, 092127.
16. K.-i. Ishibashi, Y. Kimura and M. Niwano, *J. Appl. Phys.*, 2008, **103**, 094507.
17. Y. W. Zhu, T. Song, F. T. Zhang, S. T. Lee and B. Q. Sun, *Appl. Phys. Lett.*, 2013, **102**, 113504.
18. Y. Li, W. Huang, H. Huang, C. Hewitt, Y. Chen, G. Fang and D. L. Carroll, *Sol. Energy*, 2013, **90**, 51.
19. A. Saeki, M. Tsuji, S. Yoshikawa, A. Gopal and S. Seki, *J. Mater. Chem. A*, 2014, **2**, 6075.
20. J. C. Ribierre, L. Zhao, S. Furukawa, T. Kikitsu, D. Inoue, A. Muranaka, K. Takaishi, T. Muto, S. Matsumoto, D. Hashizume, M. Uchiyama, P. Andre, C. Adachi and T. Aoyama, *Chem. Comm.*, 2015, **51**, 5836.
21. W. Shao, H. Dong, L. Jiang and W. Hu, *Chem. Sci.*, 2011, **2**, 590.
22. H. C. Han, C. A. Tseng, C. Y. Du, A. Ganguly, C. W. Chong, S. B. Wang, C. F. Lin, S. H. Chang, C. C. Su, J. H. Lee, K. H. Chen and L. C. Chen, *J. Mater. Chem.*, 2012, **22**, 22899.
23. C. Liu, Y. Xu and Y.-Y. Noh, *Mater. Today*, 2015, **18**, 79.
24. D. J. Gundlach, J. E. Royer, S. K. Park, S. Subramanian, O. D. Jurchescu, B. H. Hamadani, A. J. Moad, R. J. Kline, L. C. Teague, O. Kirillov, C. A. Richter, J. G. Kushmerick, L. J. Richter, S. R. Parkin, T. N. Jackson and J. E. Anthony, *Nat. Mater.*, 2008, **7**, 216.
25. M. Campoy-Quiles, T. Ferenczi, T. Agostinelli, P. G. Etchegoin, Y. Kim, T. D. Anthopoulos, P. N. Stavrinou, D. D. C. Bradley and J. Nelson, *Nat. Mater.*, 2008, **7**, 158.
26. Y. Yao, J. Hou, Z. Xu, G. Li and Y. Yang, *Adv. Funct. Mater.*, 2008, **18**, 1783.
27. J. Jo, S.-I. Na, S.-S. Kim, T.-W. Lee, Y. Chung, S.-J. Kang, D. Vak and D.-Y. Kim, *Adv. Funct. Mater.*, 2009, **19**, 2398.
28. S. S. van-Bavel, E. Sourty, G. de With and J. Loos, *Nano Lett.*, 2009, **9**, 507.
29. E. J. W. Crossland, K. Rahimi, G. Reiter, U. Steiner and S. Ludwigs, *Adv. Funct. Mater.*, 2011, **21**, 518.
30. M. S. Su, C. Y. Kuo, M. C. Yuan, U. S. Jeng, C. J. Su and K. H. Wei, *Adv. Mater.*, 2011, **23**, 3315.
31. Y. Vaynzof, D. Kabra, L. Zhao, L. L. Chua, U. Steiner and R. H. Friend, *ACS Nano*, 2011, **5**, 329.
32. Y. Liu, C. C. Chen, Z. Hong, J. Gao, Y. Michael Yang, H. Zhou, L. Dou, G. Li and Y. Yang, *Sci. Rep.*, 2013, **3**, 3356.
33. M. Kim, J.-H. Kim, H. H. Choi, J. H. Park, S. B. Jo, M. Sim, J. S. Kim, H. Jinnai, Y. D. Park and K. Cho, *Adv. Energy Mater.*, 2014, **4**, 1300612.
34. B. A. Collins, Z. Li, J. R. Tumbleston, E. Gann, C. R. McNeill and H. Ade, *Adv. Energy Mater.*, 2013, **3**, 65.
35. K. Sun, Z. Xiao, E. Hanssen, M. F. G. Klein, H. H. Dam, D. Pfaff, D. Gerthsen, W. W. H. Wong and D. J. Jones, *J. Mater. Chem. A*, 2014, **2**, 9048.
36. J. R. Tumbleston, B. A. Collins, L. Yang, A. C. Stuart, E. Gann, W. Ma, W. You and H. Ade, *Nat. Phot.*, 2014, **8**, 385.
37. P. G. Karagiannidis, N. Kalfagiannis, D. Georgiou, A. Laskarakis, N. A. Hastas, C. Pitsalidis and S. Logothetidis, *J. Mater. Chem.*, 2012, **22**, 14624.
38. Z. Xu, L.-M. Chen, G. Yang, C.-H. Huang, J. Hou, Y. Wu, G. Li, C.-S. Hsu and Y. Yang, *Adv. Funct. Mater.*, 2009, **19**, 1227.
39. D. S. Germack, C. K. Chan, R. J. Kline, D. A. Fischer, D. J. Gundlach, M. F. Toney, L. J. Richter and D. M. DeLongchamp, *Macromolecules*, 2010, **43**, 3828.
40. M. R. Hammond, R. J. Kline, A. A. Herzing, L. J. Richter, D. S. Germack, H. W. Ro, C. L. Soles, D. A. Fischer, T. Xu, L. Yu, M. F. Toney and D. M. Delongchamp, *ACS Nano*, 2011, **5**, 8248.
41. T. Takano, H. Masunaga, A. Fujiwara, H. Okuzaki and T. Sasaki, *Macromolecules*, 2012, **45**, 3859.
42. C. de Gracia Lux, B. Donnio, B. Heinrich and M. P. Krafft, *Langmuir*, 2013, **29**, 5325.
43. M. Brinkmann and P. Rannou, *Adv. Funct. Mater.*, 2007, **17**, 101.
44. Y. Q. Tang and C. R. McNeill, *J. Polym. Sci. B Polym. Phys.*, 2013, **51**, 403.
45. W. Chen, T. Xu, F. He, W. Wang, C. Wang, J. Strzalka, Y. Liu, J. G. Wen, D. J. Miller, J. H. Chen, K. L. Hong, L. P. Yu and S. B. Darling, *Nano Lett.*, 2011, **11**, 3707.
46. D. S. Germack, C. K. Chan, B. H. Hamadani, L. J. Richter, D. A. Fischer, D. J. Gundlach and D. M. DeLongchamp, *Appl. Phys. Lett.*, 2009, **94**, 233303.
47. M. Campoy-Quiles, M. I. Alonso, D. D. C. Bradley and L. J. Richter, *Adv. Funct. Mater.*, 2014, **24**, 2116.
48. S. B. Dkhil, D. Duché, M. Gaceur, A. K. Thakur, F. B. Aboura, L. Escoubas, J.-J. Simon, A. Guerrero, J. Bisquert, G. Garcia-Belmonte, Q. Bao, M. Fahlman, C. Videlot-Ackermann, O. Margeat and J. Ackermann, *Adv. Energy Mater.*, 2014, **4**, 1400805.
49. M. Lenes, L. J. A. Koster, V. D. Mihailetchi and P. W. M. Blom, *Appl. Phys. Lett.*, 2006, **88**, 243502.
50. D. W. Sievers, V. Shrotriya and Y. Yang, *J. Appl. Phys.*, 2006, **100**, 114509.
51. A. Guerrero, N. F. Montcada, J. Ajuria, I. Etxebarria, R. Pacios, G. Garcia-Belmonte and E. Palomares, *J. Mater. Chem. A*, 2013, **1**, 12345.
52. R. Betancur, P. Romero-Gomez, A. Martinez-Otero, X. Elias, M. Maymo and J. Martorell, *Nat. Phot.*, 2013, **7**, 995.
53. S. D. Oosterhout, M. M. Wienk, S. S. van Bavel, R. Thiedmann, L. J. Koster, J. Gilot, J. Loos, V. Schmidt and R. A. Janssen, *Nat. Mater.*, 2009, **8**, 818.
54. A. J. Moulé, J. B. Bonekamp and K. Meerholz, *J. Appl. Phys.*, 2006, **100**, 094503.
55. C. H. To, A. Ng, Q. Dong, A. B. Djurisic, J. A. Zapien, W. K. Chan and C. Surya, *ACS Appl. Mater. Interfaces*, 2015, **7**, 13198.
56. B. Huang, E. Glynos, B. Frieberg, H. Yang and P. F. Green, *ACS Appl. Mater. Interfaces*, 2012, **4**, 5204.
57. C. Gravalidis, A. Laskarakis and S. Logothetidis, *Eur. Phys. J.-Appl. Phys.*, 2009, **46**, 12505.
58. T. Ino, T. Asano, T. Fukuda, K. Ueno and H. Shirai, *Jpn. J. Appl. Phys.*, 2011, **50**, 081603.
59. A. Ng, C. H. Li, M. K. Fung, A. B. Djurišić, J. A. Zapien, W. K. Chan, K. Y. Cheung and W.-Y. Wong, *J. Phys. Chem. C*, 2010, **114**, 15094.
60. T. Johansson, L. A. A. Pettersson and O. Inganas, *Synt. Met.*, 2002, **129**, 269.
61. E. Burstein, *Phys. Rev.*, 1954, **93**, 632.
62. B. R. Bennett, R. A. Soref and J. A. Del Alamo, *IEEE J. Quantum Electron.*, 1990, **26**, 113.
63. G. Lakhwani, R. F. H. Roijmans, A. J. Kronemeijer, J. Gilot, R. A. J. Janssen and S. C. J. Meskers, *J. Phys. Chem. C*, 2010, **114**, 14804.
64. A. R. S. Kandada, S. Guarnera, F. Tassone, G. Lanzani and A. Petrozza, *Adv. Funct. Mater.*, 2014, **24**, 3094.
65. T. Takasaki, Y. Kuwana, T. Takahashi and S. Hayashida, *J. Polym. Sci. A Polym. Chem.*, 2000, **38**, 4832.
66. J. W. Kang, J. P. Kim, W. Y. Lee, J. S. Kim, J. S. Lee and J. J. Kim, *J. Lightwave Technol.*, 2001, **19**, 872.
67. H.-J. Lee, E.-M. Lee, M.-H. Lee, M.-C. Oh, J.-H. Ahn, S. G. Han and H. G. Kim, *J. Polym. Sci. A Polym. Chem.*, 1998, **36**, 2881.
68. T. Matsuura, M. Ishizawa, Y. Hasuda and S. Nishi, *Macromolecules*, 1992, **25**, 3540.
69. J. Guo, P. André, M. Adam, S. Panyukov, M. Rubinstein and J. M. DeSimone, *Macromolecules*, 2006, **39**, 3427.
70. P. Andre, S. L. Folk, M. Adam, M. Rubinstein and J. M. DeSimone, *J. Phys. Chem. A*, 2004, **108**, 9901.

71. P. Andre, P. Lacroix-Desmazes, D. K. Taylor and B. Boutevin, *J. Supercrit. Fluids*, 2006, **37**, 263.
72. P. Lacroix-Desmazes, P. André, J. M. DeSimone, A.-V. Ruzette and B. Boutevin, *J. Polym. Sci. Pol. Chem.*, 2004, **42**, 3537.
73. D. Rae Kim, W. Cha and W.-k. Paik, *Synt. Met.*, 1997, **84**, 759.
74. D. Kim, Duckhwan Lee and W.-k. Paik, *Bull. Korean Chem. Soc.*, 1996, **17**, 707.
75. M. T. Giacomini, L. M. M. de Souza and E. A. Ticianelli, *Surf. Scie.*, 1998, **409**, 465.
76. S. V. Kesava, R. Dhanker, D. R. Kozub, K. Vakhshouri, U. H. Choi, R. H. Colby, C. Wang, A. Hexemer, N. C. Giebink and E. D. Gomez, *Chem. Mater.*, 2013, **25**, 2812.
77. L. A. A. Pettersson, L. S. Roman and O. Inganäs, *J. Appl. Phys.*, 1999, **86**, 487.
78. Z. He, C. Zhong, S. Su, M. Xu, H. Wu and Y. Cao, *Nat. Phot.*, 2012, **6**, 593.
79. Q. Lin, A. Armin, R. C. R. Nagiri, P. L. Burn and P. Meredith, *Nat. Phot.*, 2014, **9**, 106.
80. H. Hansel, H. Zettl, G. Krausch, R. Kisselev, M. Thelakkat and H. W. Schmidt, *Adv. Mater.*, 2003, **15**, 2056.